

Detection and Estimation of Equatorial Spread F Scintillations Using Synthetic Aperture Radar

Jun Su Kim, Konstantinos P. Papathanassiou, *Fellow, IEEE*, Hiroatsu Sato, and Shaun Quegan, *Member, IEEE*

Abstract—A significant amount of the data acquired by sun-synchronous space-borne low-frequency synthetic aperture radars (SARs) through the postsunset equatorial sector are distorted by the ionospheric scintillations due to the presence of plasma irregularities and their zonal and vertical drift. In the focused SAR images, the distortions due to the postsunset equatorial ionospheric scintillations appear in the form of amplitude and/or phase “stripe” patterns of high spatial frequency aligned to the projection of the geomagnetic field onto the SAR image plane. In this paper, a methodology to estimate the height and the drift velocity of the scintillations from the “stripe” patterns detected in the SAR images is proposed. The analysis is based on the fact that the zonal and vertical drift of the plasma irregularities are, at the equatorial zone, perpendicular to the geomagnetic field which is almost parallel aligned to the orbit. The methodology takes advantage of the time lapse and change of imaging geometry across azimuth subapertures. The obtained height estimates agree well with the reference measurements and independent estimates reported in the literature, while the drift velocities appear slightly overestimated. This can be attributed to a suboptimum geometry configuration but also to a decoupling of the ambient ionosphere and the plasma irregularities.

Index Terms—Ionosphere, scintillations, synthetic aperture radar (SAR).

I. INTRODUCTION

AS THE ionization by solar radiation turns back with sunset, plasma irregularities are often generated in the postsunset sector of the equatorial ionosphere. While at lower altitudes the recombination reduces the number of free electrons, at higher altitudes the number of electrons remains high forming a plasma density gradient. This Rayleigh–Taylor-like instability along the steep plasma density gradient develops and amplifies further forming ascending regions of depleted plasma, known as plasma bubbles. The irregular plasma density distribution is associated with a variation of the refraction

index, so that microwaves propagating through the postsunset equatorial ionosphere experience scintillation [1], [2].

The electric field and the dynamo driven by the neutral wind in the equatorial E and F regions induce zonal drifts of ionospheric plasma. The drift direction alternates diurnally [3]: In the night sector, the drift is directed eastward, while in the day sector westward. The net drift is faster than earth’s rotation, and is therefore referred as superrotation [4]. In order to improve the understanding on the electric field in the ionosphere and the F region dynamo, the zonal drift of the ionosphere in the equatorial sector has been observed by ground-based radars (e.g., the Jicamarca Radar Observatory) [5] as well as satellite configurations (e.g., NASA’s Dynamics Explorer or Atmospheric Explorer) [4].

The plasma bubbles at the postsunset equatorial sector are extremely elongated and aligned to the geomagnetic field [6]–[8]. At the same time, close to equator, the usual sun-synchronous SAR orbits run fairly parallel to the geomagnetic field so that the plasma irregularities are aligned more or less parallel to the azimuth direction. This induces a twofold effect on SAR data. As the alignment of the irregularities is perpendicular to the LOS, the ionospheric irregularities (thus, the variation of refraction index) act as weak diffraction grating on the transmitted and received SAR pulses, so that amplitude diffraction patterns appear after range focusing. The orientation of the diffraction effects parallel to the azimuth direction prevents the diffraction patterns to be smeared out during the azimuth focusing, so that they appear well preserved in the final focused image. The phenology, geometry and statistics of the detected amplitude, and phase “stripe” patterns are discussed and interpreted in a number of recent studies [6], [7], [9].

For conventional space-borne SAR configurations operating at L-band ($\lambda \sim 23.6$ cm), the synthetic aperture is on the order of about 20 km (corresponding to an azimuth resolution on the order of 5 m) and takes approximately 3 s to be realized. Within these 3 s, the line-of-sight (LOS) connecting SAR and the scatterer is changing. In according, the ionospheric signature in the SAR images is affected by the time lapse and the change of parallax (associated with the change in LOS) along the synthetic aperture. The parallax effect is tested in [10] for the ionospheric height estimation. In this paper, a methodology that makes use of the ionospheric signature to estimate both of the height and the velocity of zonal drifts is proposed. In Section II, the equatorial F region ionosphere and its effect on the amplitude and phase of SAR data are discussed. The methodology to estimate the velocity of the ionospheric drift and the altitude of the ionosphere from

Manuscript received December 30, 2016; revised May 7, 2017; accepted June 13, 2017. This work was supported in part by the European Space Agency’s BIOMASS mission project and in part by the Helmholtz Alliance Remote Sensing and Earth System Dynamics through the Initiative and Networking Fund of the Helmholtz Association. (*Corresponding author: Jun Su Kim.*)

J. S. Kim and K. P. Papathanassiou are with the German Aerospace Center (DLR-HR), Microwaves and Radar Institute, 82234 Wessling, Germany (e-mail: junsu.kim@dlr.de; kostas.papathanassiou@dlr.de).

H. Sato is with the German Aerospace Center (DLR-KN), Institute of Communication and Navigations, 17235 Neustrelitz, Germany (e-mail: hiroatsu.sato@dlr.de).

S. Quegan is with the Centre for Terrestrial Carbon Dynamics, The University of Sheffield, Sheffield S3 7RH, U.K. (e-mail: s.quegan@sheffield.ac.uk).

Color versions of one or more of the figures in this paper are available online at <http://ieeexplore.ieee.org>.

Digital Object Identifier 10.1109/TGRS.2017.2731943

SAR data is introduced and analyzed in Section III. The analysis is based on the geometrical representation rather than on a full simulation of wave propagation in/through the ionosphere [7], [9]. The method is applied on real SAR data, and the obtained results are validated in Section IV. Finally, conclusions are drawn in Section V.

II. STRIPES

A. Drift and Irregularities of the F Region Ionosphere

The equatorial F region ionosphere is characterized by zonal and vertical drift motion of plasma. Plasma flows are governed by electromagnetic fields, and the $\vec{E} \times \vec{B}$ drift force moves the plasma perpendicular to the imposed electric and geomagnetic field. The drift motion has a diurnal variation in flow direction and magnitude: in general, the zonal drift is westward during day time and eastward during night time. In the equatorial region, the night time eastward drift is related to the vertically downward direction of the electric field in the northward magnetic field [3].

Ground-based incoherent radar measurements have extensively been used to observe the dynamics of the equatorial F region over Jicamarca in Peru. For quiet time ionosphere, the eastward drift peak speed in the premidnight sector is typically about 100 m/s while the daytime drifts usually peak at 40 m/s [5], [11]. Satellite measurements, at altitudes, about 400 km agree with the general behavior of zonal drift observed by the ground-based radar measurements both in magnitude and in flow direction. *In situ* measurements, however, tend to observe slightly higher values than ground radar [4], [12]. Recent measurements show that the premidnight enhancement of zonal velocity is also common in other equatorial longitudes [12]. Incoherent scatter radar measurements at Jicamarca have also indicated the westward flow at heights below the F2 peak [5].

As already discussed, plasma density irregularities are triggered and developed in the postsunset equatorial F region. These density structures cause forward scattering of radio signals known as scintillation. When the plasma irregularities are fully developed, the scintillation patterns are expected to flow along the ambient zonal drift motions. Using very high-frequency receivers, Bhattacharyya *et al.* [13] concluded that the irregularities in observed amplitude scintillations are confined in a thin-layer of bottom side of the F region of equatorial zone on magnetically quiet day. The westward velocity of ionospheric irregularities at midnight has been verified for magnetically quiet days at 50–100 km altitude in the South American sector by means of GPS L1 signals [14].

B. Geomagnetic Field on SAR

Plasma irregularities are aligned to the geomagnetic field, and appear on SAR images as parallel “stripe” patterns in amplitude and/or phase [6], [7]. The direction of the stripes is determined by the projection of the geomagnetic field onto the SAR image. Assuming a thin ionospheric layer at altitude h_{iono} , the magnetic field and, consequently, the plasma irregularities are projected along the propagation vector $\vec{\kappa}$

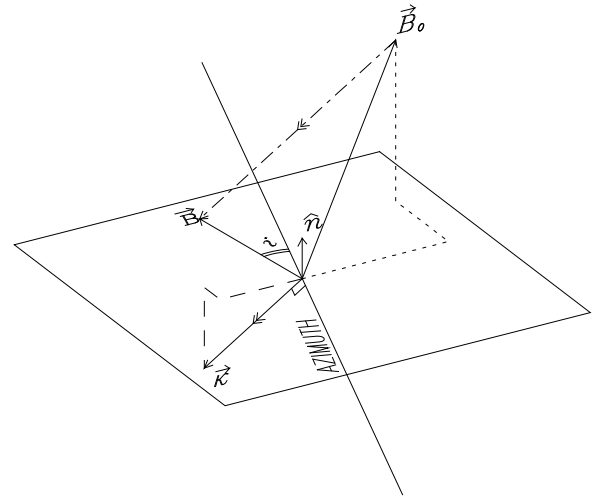


Fig. 1. Geomagnetic field and SAR imaging geometry. The vector \vec{B}_0 is the original magnetic field vector, $\hat{\kappa}$ is the unit propagation vector, \hat{n} is surface normal of horizontal ionospheric layer (assumed to be plane), and \vec{B} is the projection of \vec{B}_0 along $\hat{\kappa}$ on to the ionospheric layer. The angle between the azimuth direction and \vec{B} is i , and is, in this paper, referred as this paper the geomagnetic field angle.

onto the ionospheric thin layer. The projection of original geomagnetic field \vec{B}_0 onto the horizontal layer along $\vec{\kappa}$ is

$$\vec{B} = \vec{B}_0 - \frac{\hat{n} \cdot \vec{B}_0}{\hat{n} \cdot \hat{\kappa}} \hat{\kappa} \quad (1)$$

where \hat{n} is unit normal vector to the horizontal layer, and $\hat{\kappa} = \vec{\kappa}/|\vec{\kappa}|$ is the unit propagation vector. The geometry of (1) is demonstrated in Fig. 1. The projected magnetic component \vec{B} will be called, in the following, geomagnetic field. Note that $\vec{B} \cdot \hat{n} = 0$. The angle between the projected geomagnetic field \vec{B} and the azimuth direction will be referred as the geomagnetic field angle i . It is the angle measured from the azimuth direction (\vec{v}_{sat}) to the projected geomagnetic field (\vec{B}), where \vec{v}_{sat} is the velocity of the SAR antenna and $\vec{v}_{\text{sat}} \cdot \hat{\kappa} = 0$ (zero-squint). The sign is arbitrary. In this paper, however, for the right-looking geometry, the sign is assigned to be negative in the northern, and positive in southern hemisphere. It is clock-wise sensed, and the orbit direction (i.e., ascending or descending) does not matter. In left-looking geometry, i should be measured in counterclockwise to keep the definition of sign in each of the hemispheres as in the right-looking geometry.

Besides the geomagnetic field \vec{B}_0 which varies depending on the geographic position and the height of the ionospheric layer (h_{iono}), the orbit of satellite and the imaging direction $\hat{\kappa}$ determine the geomagnetic field angle i . As the orbit inclination of the satellite is confined to be sun-synchronous, the major factor deciding the magnitude of i is the inclination of the geomagnetic field (i.e., the magnetic dip). At the northern hemisphere, the geomagnetic field is looking down toward the ground. In the SAR geometry, the projection along $\vec{\kappa}$ brings the head of \vec{B} toward the orbit on the horizontal plane, while in the southern hemisphere to the opposite direction (see Fig. 1). This is regardless of whether the sensor looks left or right or whether the satellite is in an ascending or descending orbit.

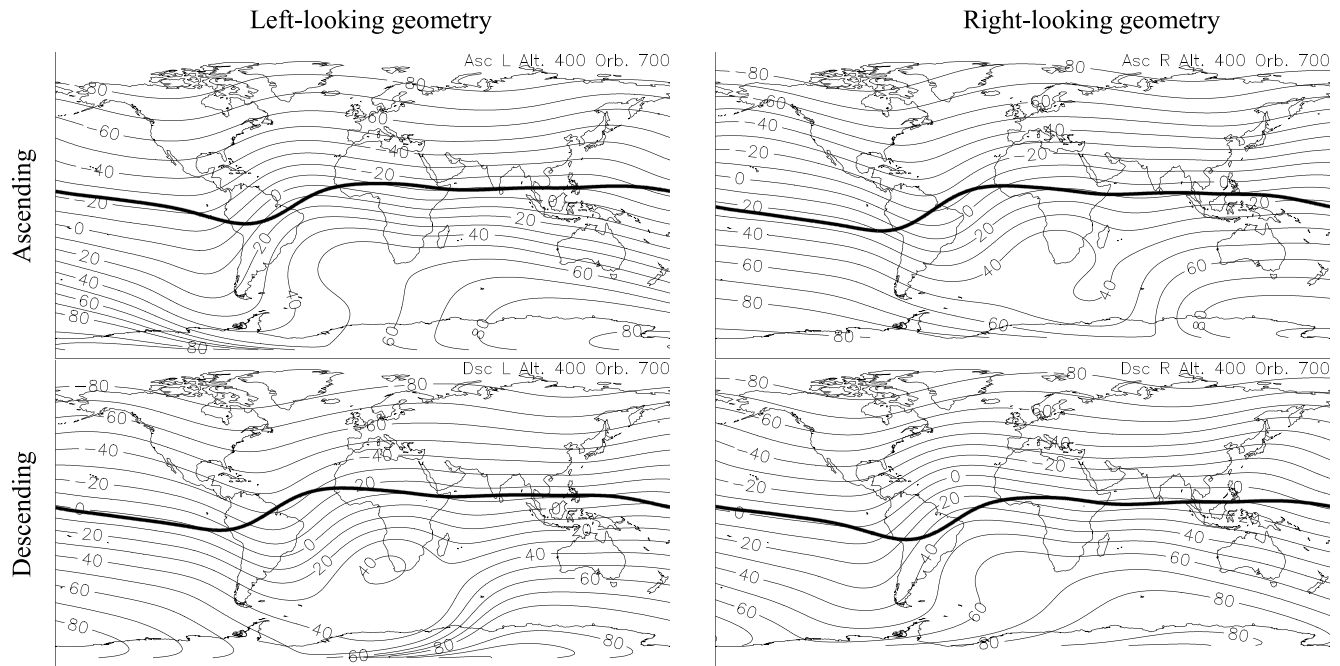


Fig. 2. Geomagnetic field angles for ascending/descending orbits and left-right-looking geometries. The orbit altitude is 700 km and the magnetic field is estimated at 400-km altitude. The orbit inclination is 98° and off-nadir angle is 30° . The thick black lines indicate where $B \cdot \hat{k} = 0$. The geomagnetic field is calculated from the International Geomagnetic Reference Field [15].

Fig. 2 shows the global distribution of the geomagnetic field angle for a sun-synchronous low earth orbit at 700-km altitude, off-nadir angle of 30° in left- and right-looking geometries, for ascending and descending orbits. The ionospheric layer is assumed at 400-km altitude. The geomagnetic field is calculated from the International Geomagnetic Reference Field [15]. The change of the sign in the northern and southern hemispheres is evident: with changing geographic latitude the contours are widely parallel to each other, but not always. The left-looking ascending and the right-looking descending cases show similar patterns, the same is the case for the right-looking ascending and left-looking descending cases.

There is another factor related to the geomagnetic field and imaging geometry: The Faraday rotation is proportional to $B_0 \cdot \hat{k}$, and differs from the geomagnetic field angle given by (1). The bold black lines in Fig. 2 indicate where $B_0 \cdot \hat{k} = 0$, and are different from the zero-geomagnetic field angle lines: the difference can be up to almost 40° . This allows the estimation of absolute TEC from Faraday rotation measurements using fully polarimetric observations of which behaviors can be compared with the “stripe” patterns and their displacements. In this paper, however, we did not perform this analysis due to the lack of appropriate fully polarimetric data sets complemented by the simultaneous ground-based measurements of ionospheric disturbances.

C. Plasma Irregularities and Stripes on SAR

For each individual pulse transmitted and received by the SAR, the plasma irregularities induce undulations on the amplitude and phase of its envelope. This can be understood as diffraction experienced as the pulses propagate through the irregular medium. Provided that the geomagnetic field angle is

not zero, the undulations of amplitude and phase are smeared by the azimuth compression [7]. The smearing becomes weaker when the geomagnetic field angle becomes smaller, but also when a reduced synthetic aperture is used. Indeed, when using only a part of azimuth spectra (i.e., azimuth subband) the contrast of the “stripe” pattern is stronger.

Furthermore, normalizing the subband power image ($\sigma_{0,\text{sub}}$) by using the full-band power ($\sigma_{0,\text{full}}$) cancels out the ground backscatter and leaves only the undulation of the “stripe” pattern induced by the ionosphere. This process is possible first because it is safe to assume that the backscatter power from most natural scatterers does not vary strongly across the synthetic aperture. Second, as the stripes are sharpened in the subband power images, the “stripe” patterns in full-band and in subband are not identical. Moreover, the stripes in the individual azimuth subband images appear displaced in the range direction depending on the look-direction of the azimuth subband, as it will be discussed later. The ratio $\sigma_{0,\text{sub}}/\sigma_{0,\text{full}}$ suppresses the inhomogeneous ground backscatter and highlights the “stripe” pattern.

Fig. 3 shows three example data sets acquired by the Japanese Advanced Land Observation Satellite (ALOS) Phase-Arrayed L-band SAR (PALSAR). The top row shows the full bandwidth images, i.e., $\sigma_{0,\text{full}}$, the middle row shows the images corresponding to the 1/16th of the total bandwidth, i.e., $\sigma_{0,\text{sub}}$, and the bottom row shows the normalized subband power ($\sigma_{0,\text{sub}}/\sigma_{0,\text{full}}$) images. The images on the left column are acquired over the Amazon basin (scene ID ALPSRP115537120 acquired on March 26th, 2008), the ones in the center over Nigeria (ALPSRP233080150 acquired on June 9th, 2010), and the right ones over Ethiopia (ALPSRP211770210 acquired on January 14th, 2010). The ionospheric “stripe” pattern becomes more subtle from left

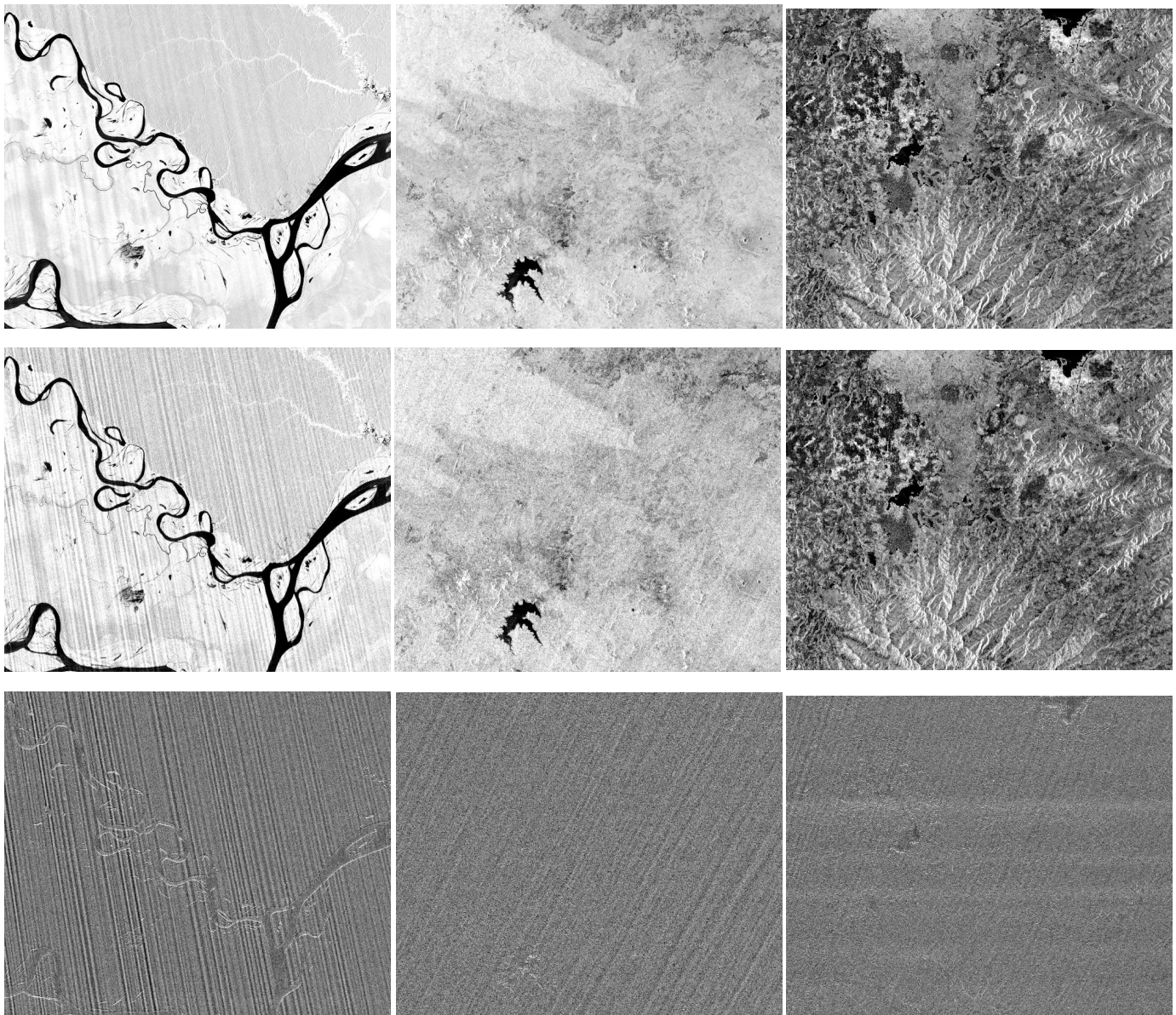


Fig. 3. Examples of “stripe” patterns in equatorial SAR acquisitions (Left) Amazon, (Center) Nigeria, and (Right) Ethiopia. (Top) Full-band power images, (Middle) Power images of 1/16th of azimuth spectra (subband power images), and (Bottom) 1/16th subband power images normalized to full-band power.

to right. In the Amazon scene, the stripes are visible in $\sigma_{0,\text{full}}$, and sharpen in $\sigma_{0,\text{sub}}$ and $\sigma_{0,\text{sub}}/\sigma_{0,\text{full}}$. In the Nigeria scene, the stripes are not visible in $\sigma_{0,\text{full}}$, become visible in $\sigma_{0,\text{sub}}$ and clear in $\sigma_{0,\text{sub}}/\sigma_{0,\text{full}}$. In the heterogeneous Ethiopia scene, the stripes are only visible when the ground backscatter components are normalized out (i.e., in $\sigma_{0,\text{sub}}/\sigma_{0,\text{full}}$). This allows us to assume that much more equatorial postsunset low-frequency SAR acquisitions bear scintillations than expected.

D. Topography

It is not only the wide azimuth beamwidth and the spatial heterogeneity of the radar reflectivity in a scene that obscures the identification of the ionospheric “stripe” pattern, but also the terrain topography. The “stripe” pattern is modulated by the variation in range distance (i.e., delay) induced by the topography variation, and becomes distorted as a consequence of layover and foreshortening effects.

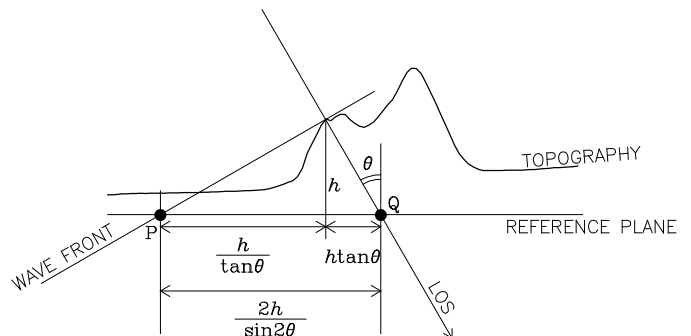


Fig. 4. Geometry for topography correction.

The geometric distortion of the ionospheric pattern can be compensated when the incidence angle θ and the altitude of the scatterer h (thus, the foreshortening factor $h/\tan\theta$) are known, for example by using external DEMs. The geometry is shown in Fig. 4: in the absence of topography, the pulses propagate

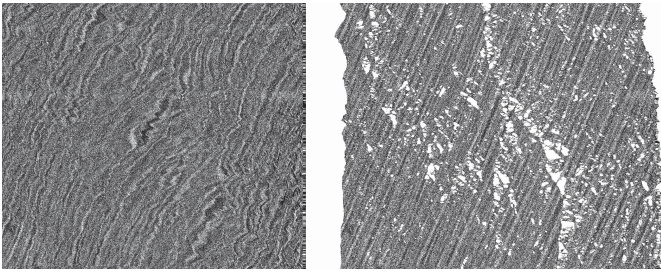


Fig. 5. Normalized subband power images (Left) before and (Right) after topographic compensation over equatorial Andes (Scaled within 4 dB).

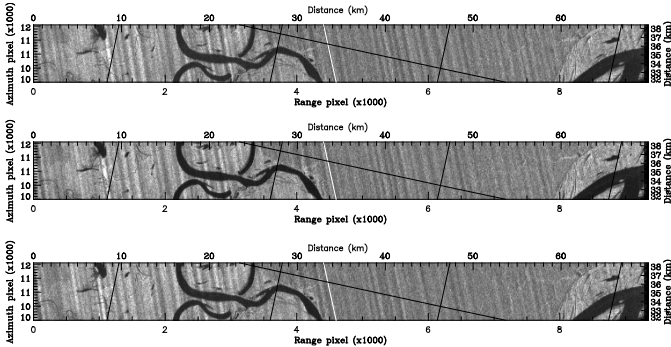


Fig. 6. 1/16th subband power images: (Top) 3rd subband, (Middle) 8th subband, and (Bottom) 13th subband. The displacement of the “stripe” pattern is clearly visible.

along the LOS until the reference plane and the scatterer is imaged at the position Q . In the presence of topography that lifts (or sinks) the scatterer above (or below) the reference plane, the image position should be shifted toward the far (or near) range as much as $2h/\sin 2\theta$, in order to compensate for the foreshortening of the ionospheric stripes due to the topography. Note that this is different from ortho-rectification where every scatterer is dropped vertically to the reference plane. In the proposed topography compensation, the scatterers are projected “along the LOS,” i.e., \hat{k} , to the reference plane. This situation is the same as in (1), where replacing the thin ionospheric layer with the reference plane.

Fig. 5 shows an example of topographic compensation in an ALOS PALSAR scene acquired in the equatorial Andes (scene ID ALPSRP218086950 acquired on February 27th, 2010 at 3:57:24 UTC). The “stripe” pattern is clearly deformed by foreshortening/layover effects but after the topographic compensation, the linearity of the pattern is recovered. For the correction, the SRTM 90 DEM [16] has been used. The white holes appear in the layover areas. Besides “straightening” the ionospheric stripes and increasing their detection rate, the topographic correction is essential when estimating the displacement of the pattern across the different azimuth sublooks as will be discussed in the following section.

III. DISPLACEMENT AND INTERPRETATION

A. Displacement

The position of equatorial “stripe” pattern changes across the images depending on the selection of the center Doppler frequency of the azimuth subband. Fig. 6 compares the power images of the 3rd, 8th, and 13th of the 16 subbands of the Amazon scene [17] each with a bandwidth of 134 Hz and centered at Doppler frequencies of 602, -67 , and -736 Hz,

respectively. In order to compare the displacement of the “stripe”-pattern relative to the background features, the full-band power is not normalized. The “stripe” patterns are moving from sublook-to-sublook toward near range; their displacement reaches up to hundreds of pixels corresponding to a few kilometres.

The Amazon scene was acquired with a pulse repetition frequency (PRF) of $f = 2141.3$ Hz, the Doppler rate of $D_r = 519$ Hz/s, and the satellite forward speed ($|\vec{v}_{\text{sat}}| = v_{\text{sat}}$) of 7.6 km/s. For a 16th subaperture, therefore, it takes $((f_{\text{PR}}/D_r)/16 \Rightarrow) 0.258$ s. The appropriate number of subbands for estimating the displacement of the “stripe” pattern is a tradeoff between spatial resolution and correlation. When too many subbands are used, the azimuth resolution becomes too low, and it becomes challenging to get a sufficient number of samples for a reliable amplitude correlation between neighboring subbands. On the other hand, a small number of subbands increases the separation of ionospheric piercing points (i.e., the intersection of the LOS and the ionosphere) and degrades the correlation between them. The use of mutually overlapping subbands is not recommended as it smears out the “stripe” pattern. In the Amazon scene, the multiplications of estimated displacement and the number of looks stay constant for the trials of using 6, 9, and 16 subbands. In the following, 16 sublooks will be used.

The displacement of the “stripe” pattern between neighboring subbands is estimated in three steps: First, each subband image is normalized using the full-band power ($\sigma_{0,\text{sub}}/\sigma_{0,\text{full}}$) as already described in Section II-C. Then, if necessary, the topography compensation is performed. And finally, the cross correlation between adjacent normalized power images is estimated

$$X_k = \frac{\sigma_{0,k-\text{sub}}}{\sigma_{0,\text{full}}} * \left(\frac{\sigma_{0,(k+1)-\text{sub}}}{\sigma_{0,\text{full}}} \right)^* \quad (2)$$

where X_k is the cross correlation between subband indexed k and $k + 1$.

Because of the strong elongation of the stripes, the cross correlation between the normalized powers is corrugated, i.e., does not show a point peak but a linear ridge oriented parallel to the stripes. Fig. 7 shows such a cross correlation example between normalized subbands. The correlation is estimated using a $40 \text{ km} \times 40 \text{ km}$ area of the scene center. Assuming a stationary ionosphere, i.e., that its altitude and drift velocity remain constant within the synthetic aperture, the cross correlation between neighboring subbands should be the same. In this case, the sum of cross correlations across all subbands $\sum_k X_k$ reduces the noise contributions. The displacement of the “stripe” pattern between neighboring subbands is then estimated by determining the displacement of the main ridge in the range direction. The direction and the displacement are estimated by means of a least square fitting to the strongest points (e.g., red dots in Fig. 7). The threshold used to detect the strongest points depends on the characteristics of the scene, e.g., the strength of the stripes, the peak power of secondary ridges, and the topography. Finally, the displacement is measured only in the range direction. For the Amazon scene in Figs. 6 and 7, the displacement is estimated to be -101 m

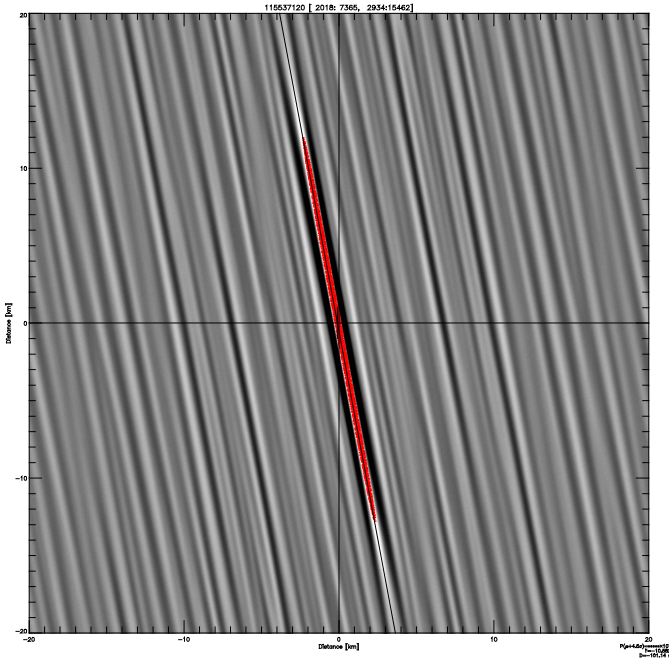


Fig. 7. Cross correlation between subbands. The red dots are strong points used to estimate the best fitting line along the primary ridge.

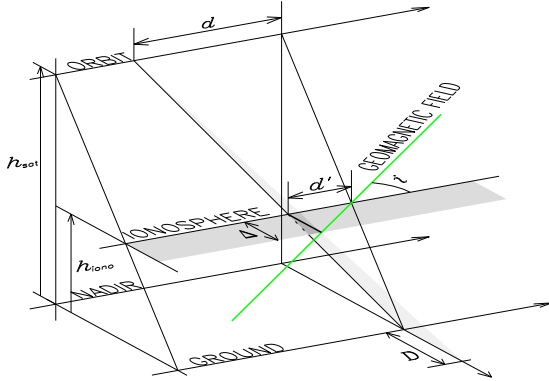


Fig. 8. Geometry for the interpretation of the range displacement of the ionospheric “stripe” pattern across different azimuth subbands.

per every 16th subband. In practice, the processed (azimuth) bandwidth of ALOS PALSAR (~ 1531 Hz) is narrower than the PRF. Among 16 subband power images ($\sigma_{0,\text{sub}}$), only the 3rd to the 14th images yield a strong enough signal after normalization. In according, 11 adjacent cross correlation estimates were summed up in Fig. 7.

It is also possible to attempt a dare-devil cross correlation directly between the 3rd and 14th azimuth subband, but in this case the correlation does not result into clear enough ridges. Assuming an ionospheric altitude at the half orbit altitude, the distance between 3rd and 14th subbands is roughly 10 km. Despite the strong elongation of the plasma irregularities, the correlation across such a distance is lower than between adjacent subbands which are only 1 km.

B. Geometric Interpretation

In the following, it is assumed that only two components of the thin-layer ionosphere contribute to the direction and the displacement of the “stripe” pattern appearing on SAR

image: 1) a static component given by the oblique geometry of the geomagnetic field \vec{B} described by the geomagnetic field angle i and 2) a dynamic component given by the component of the drift of the plasma irregularities in the range direction. Thus, for the parameterisation of the problem two parameters are needed: the altitude of the ionosphere h_{iono} that modifies \vec{B} , and the range-projected drift velocity v_{\perp} . At the same time, there are two “observables”: the angle of the stripes i' (i.e., the one estimated on the SAR image, and not the one with the geomagnetic field angle i which is estimated at the ionospheric altitude) and the displacement of the “stripe” pattern across subbands D . First, the static component is analyzed. Fig. 8 shows the geometric configuration. Let us set the position of the satellite to be as much as d behind the zero-Doppler plane. The center frequency of azimuth subband becomes $f_{\text{az}} = D_r \cdot (d/v_{\text{sat}})$. On the ionospheric layer, this distance is reduced to $d' = (h_{\text{iono}}/h_{\text{sat}}) \cdot d$. The geomagnetic field \vec{B} is placed on the ionospheric layer and forms the geomagnetic field angle i with respect to the orbit. Seen at position d , the geomagnetic field on the ionospheric plane is displaced in the range direction as much as $\Delta = \tan i \cdot d'$ with respect to the zero-Doppler position. Finally, every range displacement on the ionospheric layer is scaled by a factor $h_{\text{sat}}/(h_{\text{sat}} - h_{\text{iono}})$ in the SAR image. In according, the static displacement contribution due to parallax in the range direction is

$$D_{\text{sta}} = \frac{h_{\text{sat}} \cdot \Delta}{h_{\text{sat}} - h_{\text{iono}}} = \frac{d \cdot h_{\text{iono}}}{h_{\text{sat}} - h_{\text{iono}}} \tan i. \quad (3)$$

Similarly, the angle of the geomagnetic field i is scaled to

$$\tan i'_{\text{sta}} = \frac{h_{\text{sat}}}{h_{\text{sat}} - h_{\text{iono}}} \tan i \quad (4)$$

where i'_{sta} is angle of the geomagnetic field scaled to the ground.

The dynamic contribution acts in a more intuitive way. As the range projected drift velocity of the plasma is v_{\perp} , during the time the satellite moves along a distance d/v_{sat} , the plasma irregularities move in the range by $v_{\perp} \cdot d/v_{\text{sat}}$ on the ionospheric layer. This displacement is scaled in the SAR image to

$$D_{\text{dyn}} = d \frac{v_{\perp}}{v_{\text{sat}}} \frac{h_{\text{sat}}}{h_{\text{sat}} - h_{\text{iono}}}. \quad (5)$$

The drift of the plasma will also modify the angle of the “stripe” pattern in the SAR image, inducing an additional tangent v_{\perp}/v_{sat} component at the ionospheric altitude. On the “stripe” pattern in the SAR image this becomes

$$\tan i'_{\text{dyn}} = \frac{h_{\text{sat}}}{h_{\text{sat}} - h_{\text{iono}}} \frac{v_{\perp}}{v_{\text{sat}}}. \quad (6)$$

From (3)–(6), the displacement D and the angle of the stripes i' estimated in the SAR image can be written with respect to ionospheric altitude h_{iono} and v_{\perp} as

$$\frac{D}{d} = \frac{D_{\text{sta}} + D_{\text{dyn}}}{d} = \frac{1}{h_{\text{sat}} - h_{\text{iono}}} \left(h_{\text{iono}} \tan i + h_{\text{sat}} \frac{v_{\perp}}{v_{\text{sat}}} \right) \quad (7)$$

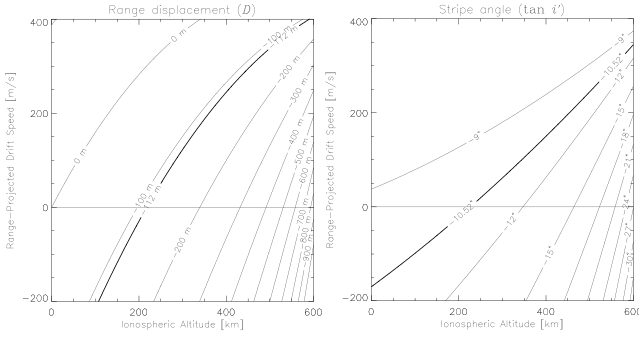


Fig. 9. Scalar field of D and $\tan i'$ for the Amazon test data. The estimates of D and $\tan i'$ indicate an ionospheric height h_{iono} around 200 km and negligible v_{\perp} .

and

$$\tan i' = \tan i'_{\text{sta}} + \tan i'_{\text{dyn}} = \frac{h_{\text{sat}}}{h_{\text{sat}} - h_{\text{iono}}} \left(\tan i + \frac{v_{\perp}}{v_{\text{sat}}} \right). \quad (8)$$

In (7), d is divided on both sides, so that (7) and (8) have the same dimension. Both (7) and (8) can be considered as the linear combinations of $\tan i$ and v_{\perp}/v_{sat} . The $\tan i$ is a geometric term primarily defined by the latitude and increases to infinity close to the polar regions (see Fig. 2). The v_{\perp}/v_{sat} term is a physical and rather small contribution, as v_{\perp} is small compared to v_{sat} . For $v_{\perp} \approx 100$ m/s, so $v_{\perp}/v_{\text{sat}} \approx 0.013$, the equivalent geomagnetic field angle i is only 0.75° . This indicates that the geometric component given by $\tan i$ is almost always dominant. The best condition for the estimation of v_{\perp} is given for small $\tan i'$ and low h_{iono} values. When $\tan i$ becomes sufficiently large compared to v_{\perp}/v_{sat} , the estimate of v_{\perp} becomes no longer reliable due to the estimation error of D and $\tan i'$, and only the height estimation remains meaningful.

Equations (7) and (8) cannot be solved analytically, as in fact $\tan i$ is a nonlinear function of h_{iono} . Instead, a numerical solution is possible in the 2-D plane defined by $\{h_{\text{iono}}, v_{\perp}\}$ and calculating the scalar fields for D and $\tan i'$, according to (7) and (8). Fig. 9 demonstrates both scalar fields for the Amazon scene. The thick curves corresponding to the measured displacement D (Left) and stripe angle i' (Right) cross at h_{iono} of 200 km and v_{\perp} of zero. This pair of $\{h_{\text{iono}}, v_{\perp}\}$ is interpreted as the estimate of altitude and the drift of the ionosphere. Subtracting (7) from (8) cancels the dynamic component, so that the difference between $(D/d) - \tan i'$ becomes a function of the ionospheric height h_{iono} only (i' is function of ionospheric height), opening way to 1-D solution search. But as it will be discussed in the following, this is valid only in a simplified Cartesian geometry.

C. Adaptation to Earth's Curvature

The geometric interpretation in Cartesian coordinates is only the first-order approximation as earth's curvature has to be considered in the space-borne SAR geometry. The effect of earth's curvature can be analyzed in the range and azimuth direction separately. In range, the curvature has to be considered in the estimation of both the stripe angle i' and the displacement D , while in azimuth the curvature has only an effect on the estimation of the stripe angle i' .

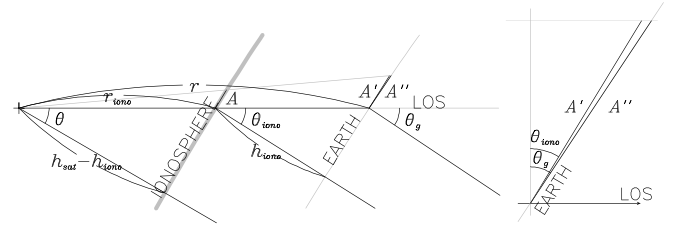


Fig. 10. Effect of earth's curvature on the SAR image geometry. h_{iono} is the ionospheric altitude (i.e., altitude to the ionospheric layer), h_{sat} is the orbit altitude, and r and r_{iono} are the distance to the ground and the ionospheric layers, respectively. (Left) For an off-nadir angle θ , the local incidence angles at the ground and at the ionospheric layers become θ_g and θ_{iono} , respectively. (Right) A displacement A on the ionosphere is projected on ground to A' and A'' with and without consideration of curvature.

In addition to the earth's curvature, the SLC images (which are regularly sampled in slant range) are resampled for a regular pixel spacing on ground range. This suppresses the bias in the stripe angle, the displacement, and the ground positioning estimates.

1) *Range Direction*: Considering the earth's curvature, the incidence angle becomes a function of the height of the reference plane (see Fig. 10), and the scaling in range given in (3)–(6) has to be modified. As well, in a non-Cartesian coordinates, the LOS distance from the ground to the ionosphere and the ionospheric altitude are no longer proportional, so that the distance from the satellite to the ionosphere r_{iono} and to the ground r are used instead of $h_{\text{sat}} - h_{\text{iono}}$ and h_{sat} , respectively. The incidence angles at the ionospheric altitude θ_{iono} and at the ground θ_g are given by

$$\frac{\sin \theta_{\text{iono}}}{R_e + h_{\text{sat}}} = \frac{\sin \theta}{R_e + h_{\text{iono}}} \\ \frac{\sin \theta_g}{R_e + h_{\text{sat}}} = \frac{\sin \theta}{R_e} \quad (9)$$

where θ is the off-nadir angle and R_e is the radius of the earth (~ 6371 km). For example, for an orbit altitude of 700 km and off-nadir angle of 30° , the incidence angle on the ionospheric layer at 400-km altitude is 31.48° , and on the earth's surface 33.71° .

Let us assume a displacement A on the ionospheric altitude in range direction (see Fig. 10) of either geometric or dynamic origin. When no curvature effect is considered, it will be projected onto ground as a displacement $A' = A \cdot r/r_{\text{iono}}$. But for a curved earth, the ground is more tilted than the ionospheric layer ($\theta_g > \theta_{\text{iono}}$), and what actually appears on ground is A'' which is given by $A' \cos \theta_{\text{iono}} = A'' \cos \theta_g$ (see zoomed-in-view in Fig. 10). In our example, A'' is about 2% larger than A' and increases rapidly for larger incidence angles. Considering curvature, a displacement A on the ionosphere is projected on the ground as much as A''

$$A'' = A \frac{r}{r_{\text{iono}}} \frac{\cos \theta_{\text{iono}}}{\cos \theta_g}. \quad (10)$$

Note that the incidence angles θ_g and θ_{iono} have been derived by using the Sine rule in (9), which is not valid on earth ellipsoid where R_e is not constant. However, in practice, $\cos \theta_g$ and $\cos \theta_{\text{iono}}$ are estimated by the inner products of \hat{k} and the normal vectors at points of interest, and are therefore free from approximation errors.

2) *Azimuth Direction*: While the satellite moves forward along its orbit in the speed of v_{sat} , its zero-Doppler plane does not translate but rotates around the axis normal to the orbital plane and passing through the center of the earth. At the ionospheric altitude, the motion velocity of the zero-Doppler plane reduces by a factor of $(R_e + h_{\text{iono}})/(R_e + h_{\text{sat}})$, and on the ground it is $R_e/(R_e + h_{\text{sat}})$. The geomagnetic field angle i is estimated on the ionospheric altitude. The ratio of the range component to the azimuth component of \vec{B} is, by definition, $\tan i$. As described in the previous section, during the imaging process, the range component is scaled, while the azimuth component is compressed by $R_e/(R_e + h_{\text{iono}})$. Accordingly, the static component of the $\tan i'$ is no longer given by (4), but

$$\tan i'_{\text{sta}} = \tan i \frac{r}{r_{\text{iono}}} \frac{\cos \theta_{\text{iono}}}{\cos \theta_g} \frac{R_e + h_{\text{iono}}}{R_e}. \quad (11)$$

Similarly, in the dynamic component of the stripe angle i' , the scaled motion of the ionosphere is further adjusted by the compression factor in the azimuth direction $R_e/(R_e + h_{\text{iono}})$

$$\tan i'_{\text{dyn}} = \frac{v_{\perp}}{v_{\text{sat}}} \frac{R_e + h_{\text{sat}}}{R_e} \frac{r}{r_{\text{iono}}} \frac{\cos \theta_{\text{iono}}}{\cos \theta_g} \quad (12)$$

where $v_{\text{sat}} \cdot R_e/(R_e + h_{\text{sat}})$ is the forward velocity of the nadir point.

Considering earth's curvature, the static component of the displacement (3) can be rewritten as

$$D_{\text{sta}} = d \tan i \frac{r - r_{\text{iono}}}{r_{\text{iono}}} \frac{\cos \theta_{\text{iono}}}{\cos \theta_g} \quad (13)$$

and the static component of stripe angle $\tan i'_{\text{sta}}$ is (11). The dynamic component of the displacement (5) becomes

$$\frac{D_{\text{dyn}}}{d} = \frac{r}{r_{\text{iono}}} \frac{\cos \theta_{\text{iono}}}{\cos \theta_g} \frac{v_{\perp}}{v_{\text{sat}}} \quad (14)$$

and the dynamic component of the stripe angle $\tan i'_{\text{dyn}}$ is given by (12). Equations (12) and (14) are no longer identical as they were in Cartesian coordinates, but proportional to each other as a function of $R_e/(R_e + h_{\text{sat}})$.

IV. RESULTS

A. Data

Two series of 27 consecutive ALOS acquisitions over the west Amazon area acquired on December 25th, 2007 and on March 30th, 2008 are analyzed in the following. Fig. 11 shows their foot-prints and the nadir track of orbit. The contour lines of the geomagnetic field angle, estimated at 400-km altitude and projected to the ground along the LOS are over-plotted. Note that the incidence angle changes from 0 to more than 70° in this map, while the incidence angle at the scene center is about 38.8° . The geomagnetic field angles shown in Fig. 2 are calculated for a fixed off-nadir angle but arbitrary local time of ascending nodes, so that Fig. 11 does not correspond to the right-looking ascending orbit shown in Fig. 2. The dashed contours in Fig. 11 are the geomagnetic dip angle at 400 km. It is evident that the geomagnetic equator (i.e., where the dip angle equals zero) does not coincide with the zero-geomagnetic field angle.

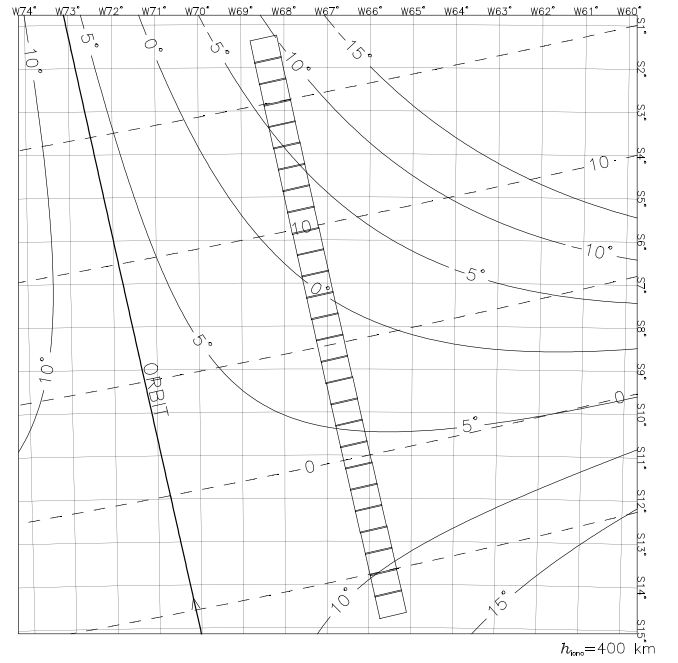


Fig. 11. Footprints and nadir-tracks of the 27 consecutive ALOS PALSAR acquisitions across Amazon. The solid contours correspond to the geomagnetic field angle, and dashed contours indicate the geomagnetic dip angles. The geomagnetic field is calculated at 400-km altitudes. Each side of the map is 1600 km.

Fig. 12 shows the power images of the two acquisitions and the phase of the interferogram formed between them. The Amazon forest is homogeneous enough that a dynamic range of only 2 dB, from -8.5 to -6.5 dB of the radar backscatter, is sufficient to illustrate the geographical features at an extent of 1600 km, with only exceptions the swamps at the very south part and the areas along the rivers characterized by either specular or dihedral backscatter. Because of this homogeneity and the flat topography, it is possible to visualize the “stripe”- patterns without normalizing the background contributions. The contrast of the stripes is stronger for the 2009 March data. The arc-shaped stripes indicate that ionospheric structures can be captured and be analyzed by means of SAR even at regional scales.

Looking on the interferogram, the correspondence of the phase patterns to the “stripe” pattern in the amplitude images is clearly visible. At L-band, a cycle of interferometric phase (i.e., 2π) corresponds to 0.43 differential TECU, indicating a differential TEC variation of about 10 TECU between the two acquisition dates. The fast variation of the phase pattern in azimuth, from the 250 to the 550 km, seems to be related to the diminishing of the “stripe” pattern visible in the December 2008 data. At the same place, the step-like jumps of the phase pattern in the range direction appear correlated with prominent stripes of the March 2009 data. In addition, there is a short stop of changing trend of the interferometric phase around -400 km, where the geomagnetic equator is. Which date's ionosphere is responsible for the background trend of the interferometric phase is ambiguous. This kind of ambiguity is intrinsic of the interferometric analysis, although it can provide differential TEC estimates at high spatial resolutions and accuracy.

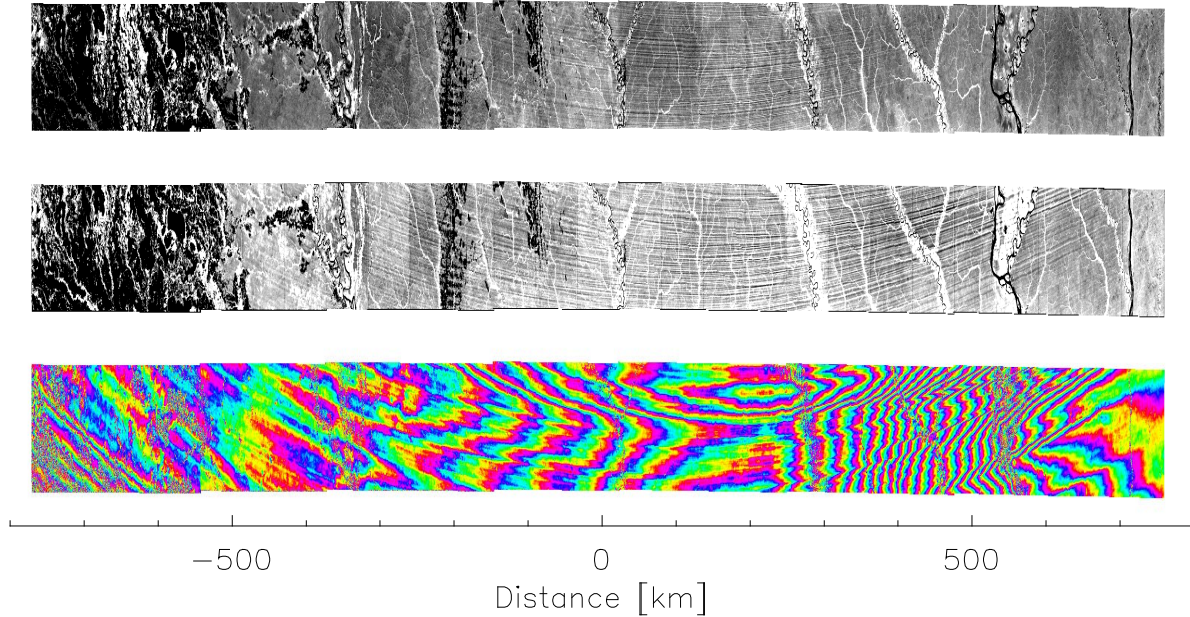


Fig. 12. Power images of the two ALOS PALSAR image stripes (each consisting of 27 consecutive scenes) acquired across Amazon on (Top) December 2008 and (Middle) March 2009. The color is from black for -8.5 dB to white for -6.5 dB. The interferometric phase of the interferogram formed between them is shown at the bottom. The images are scaled in range direction by a factor of 2.5 for better illustration of arc-shaped “stripe” pattern.

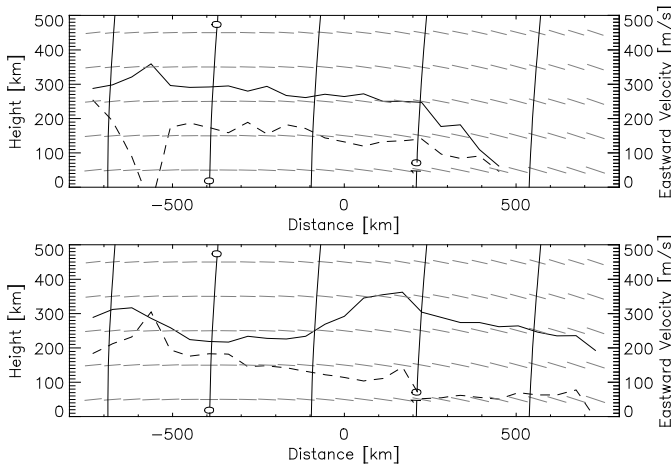


Fig. 13. Height and velocity estimation results obtained from the (Top) December 2007 and (Bottom) May 2008 data sets. The solid lines indicate height and the dashed lines indicate the eastward velocity. The line segments in the background are the projected geomagnetic field lines onto the vertical plane. The geomagnetic dip angles are indicated by the contours.

B. Results

Despite the variation of the geometry across the whole range of the 1600 km, the proposed methodology provides robust velocity and height estimates for both acquisitions. The results are shown in Fig. 13. The height estimates are indicated by the solid, and the range-projected drift velocity estimates by the dashed lines. The gray lines in the background indicate the geomagnetic field projected onto the vertical plane bearing the azimuth direction at the center of each line. The vertical contours indicate the geomagnetic dip angles. Note that the ionospheric phenomena are often symmetric with respect to the geomagnetic equator, but not with respect to the apex of the “stripe” pattern.

The height estimates are distributed between 200 and 400 km, and the velocity estimates are in most cases

less than 200 m/s. Both are physically adequate values. For the December 2008 data, the height estimates are slightly above 250 km and lower where the “stripe”-pattern diminishes. The velocity estimates are stable with values around 150 m/s with a slightly decreasing trend, and decrease rapidly just before the “stripe”-pattern disappears. This might indicate a net downward motion of the true (before the projection onto the range direction) drift velocity vector.

For the 2009 March data, the obtained height estimates vary within a range of about 150 km. The velocity estimates show in general a decreasing trend. A noteworthy point of this data set is that the estimation results can be grouped into two parts: the first part extends from -800 to 200 km: in this range the velocity estimates are decreasing, but the height estimates show a decreasing at the early half and increasing at later half with a symmetric behavior around the geomagnetic equator (zero dip angle). The second part ranges from 200 km until the end of the sequence. The height estimates decrease while the velocity estimates remain constant at far lower levels than in the first part. Looking at the power image shown in Fig. 12, one may see the interferences of “stripe” patterns of slightly different stripe angles at around 200 km become visible. This is an evidence for a multilayer structure of the ionospheric irregularities in the equatorial spread F.

C. Validation With Ground-Based Measurements

Although the Amazon data set provides ionospheric height and drift estimates in a physically plausible range and reasonable spatial distributions in a wide range of latitudes, there is no direct validation. For this, two ALOS PALSAR acquisitions, the first acquired on January 19th, 2008 at 3:50:25 (scene ID ALPSRP105766950), and the second on February 27th, 2010 at 3:57:24 UTC (scene ID ALPSRP218086950), over the Peruvian Andes, both affected

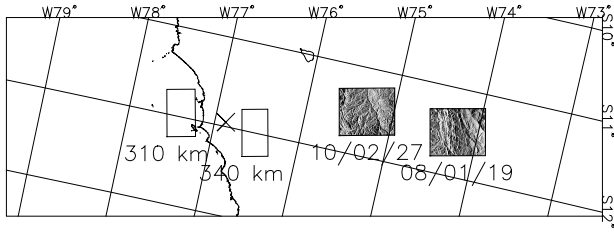


Fig. 14. Location of the two ALOS acquisitions used for the validation with the Jicamarca ground-based radar measurements. The location of JRO is indicated by the cross (×). Global self-consistent, hierarchical, high-resolution shoreline database is used for the Coastline mapping [18].

by strong amplitude “stripe” patterns, have been identified and analyzed. Their locations are shown in Fig. 14. Nearby, the Jicamarca Radio Observatory (JRO) (its location is indicated by × in Fig. 14) provides ionosonde measurements of the ionospheric altitude and drift. The data are accessed through the Global Ionospheric Radio Observatory (GIRO) [19].

The hmF2 measurements provided through GIRO are acquired by Digisonde ionogram [19] and used for the validation of the height estimates. The drift velocity measurements provided through GIRO are also derived from the Digisonde ionogram measurements [19]. Both of the height and the velocity measurements are available in a 15-min interval. For validation, five successive measurements performed around the ALOS acquisition times are used. As the ionospheric drift measurements from GIRO are provided in terms of east–west, north–south, and vertical components, they need to be projected into the side-looking radar geometry. The first step is to project the velocity vector into the ionospheric horizontal plane along the propagation vector in the same way as in (1) that leads to $\vec{v}_{\parallel} = \vec{v} - ((\hat{n} \cdot \vec{v}) / (\hat{v} \cdot \hat{k}))\hat{k}$, where \vec{v} is the measured velocity vector, and \vec{v}_{\parallel} is its projection onto the horizontal plane. In a second step its projection onto the range direction along the geomagnetic field \vec{B} is required because only the range direction displacement of the stripes is estimated, and the stripes are assumed to be aligned to the geomagnetic field line. The velocity to be compared becomes

$$\vec{v}_{\perp} = \vec{v}_{\parallel} - \frac{\vec{v}_{\parallel} \cdot \hat{a}}{B \cdot \hat{a}} \vec{B} \quad (15)$$

where $\hat{a} = ((\vec{v}_{\text{sat}}) / (|\vec{v}_{\text{sat}}|))$ is the unit vector along the azimuth direction. The values used for the validation along with the original measurements from Digisonde are shown in Table I.

Fig. 15 shows the validation results. The format is the same as in Fig. 9. The green background is the scalar solution field. The yellow band indicates the solution space for the displacement condition [i.e., sum of (13) and (14)], and the orange band indicates the solution space for the stripe angle condition [i.e., sum of (11) and (12)]. The intersection of the two solution spaces is then interpreted as the estimation of the ionospheric altitude and the range-projected drift velocity. Although the two conditions are very close to each other and quite parallel in both of two SAR acquisitions, they do intersect. While the 2008 data shows an excellent agreement between the ground measurements and the SAR-based estimation, the 2010 data do not fit the ground measurements: The drift velocity is strongly underestimated. A possible explanation for this is the

TABLE I
IONOSONDE MEASUREMENT OF JRO [16] DURING
COINCIDING ALOS ACQUISITIONS

Time	Height (km)	Eastward	Northward	Vertical	Range Projected
3:30	324.1	102.6	59.2	-39.0	76.8
3:45	337.2	98.7	39.5	-2.6	99.5
4:00	347.0				
4:15	331.1	78.9	19.7	-7.9	75.0
4:30	337.4	71.1	7.9	-9.2	65.9

Acquisition on January 19th, 2008. ALOS acquisition at 3:50:25

Time	Height (km)	Eastward	Northward	Vertical	Range Projected
3:30	324.9	90.8	-78.9	-15.8	80.7
3:45	336.1	98.7	-43.4	-17.1	88.1
4:00	393.8	98.7	-19.7	-19.7	86.7
4:15	297.8	94.7	15.8	-21.1	81.2
4:30	271.9	86.8	19.7	-22.4	72.1

Acquisition on February 27th, 2010. ALOS acquisition at 3:57:24

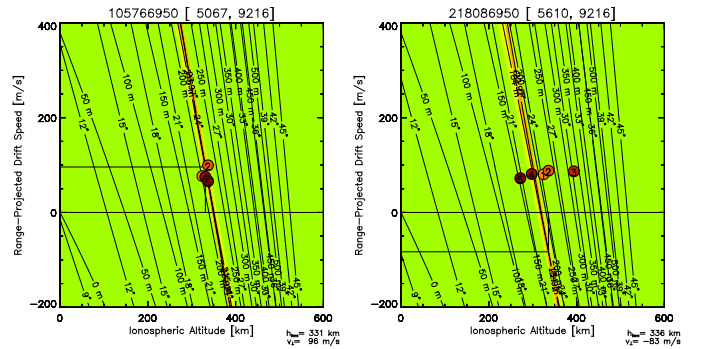


Fig. 15. Estimation of ionospheric altitude and drift speed (Left) for the 2008 scene (scene ID ALPSRP105766950) and (Right) for the 2010 scene (scene ID ALPSRP218086950). The reddish dots are the measurements from JRO performed every 15-min for an hour interval.

existence of a second ionospheric layer, which superimposes second series of “stripe” pattern and ridges with different directions on the SAR image and the cross correlation map, respectively. These perturb the estimates of the stripe angle and displacement from the cross correlation map. The possible multilayer interpretation might explain the rapid change of the ionospheric height of about 100 km observed in the Digisonde measurements (see Table I).

In order to verify the assumption of a multilayered ionospheric structure, the cross correlation map of the 2010 data is further analyzed. Indeed, the (cross correlation) map shows the interference of two “stripe” patterns with different stripe angles (see Top left image of Fig. 16), which are separable in the frequency domain (see the Top right of Fig. 16). In order to parameterise the anisotropy of the spectral power distribution, its orientation dependence is estimated (see the bottom of Fig. 16). As the cross correlation map is real numbered, only an angle between -180° and 0° is analyzed. A zoomed-in-view from -30° to -15° around the peak spectral power is shown. The spectral power is

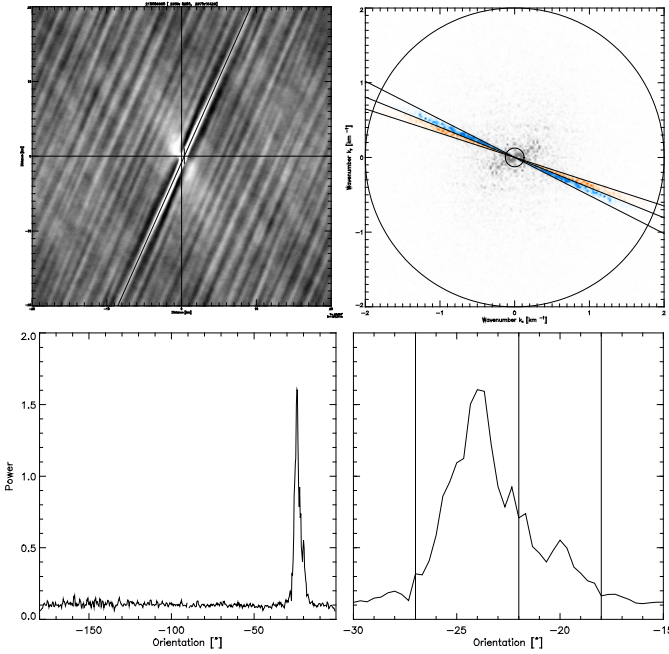


Fig. 16. (Top left) Cross correlation map, (Top right) Its Fourier transform, and (Bottom) the power distribution with respect to the orientation. The two superimposed “stripe”- patterns in the cross correlation map correspond to the two predominant orientations found at -24° and -20° . Two sectors around the local spectral power peaks indicated red and blue are used for estimating the height and velocity of the two layers.

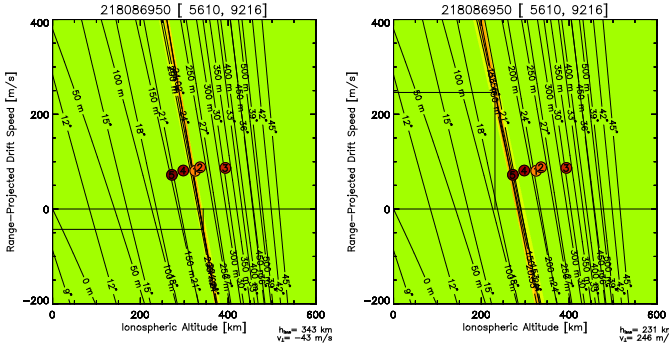


Fig. 17. Estimation of two-layer ionospheric altitude and drift speed from the 2010 scene (scene ID ALPSRP218086950) (Left) for the blue sector (layer 1) and (Right) for the red sector (layer 2) (see Fig. 15). The red dots are the measurements from JRO performed every 15-min for an hour interval.

mainly concentrated around -24° , but also a secondary peak is evident at -20° . Two pairs of sectors located around the two peaks, marked by blue and red, respectively, are inverse Fourier transformed, and then used for the height and velocity estimation, independently.

The stripes angle i' from the blue sector is -24° , and that from the red sector is -20.5° . They agree with the center orientations of each sector. The displacement estimates vary; in the blue sector, $D = 365$ m per a 16th azimuth subband, while in the red sector, $D = 274$ m. In the single-layer estimates, $i' = 24^\circ$ and $D = 361$ m, only the dominant peak power from the blue sector is represented.

The inversion results are shown in Fig. 17. The blue sector estimates the ionospheric height at $h_{\text{iono}} = 345$ km and (projected) drift velocity of $v_{\perp} = -43$ m/s. The height

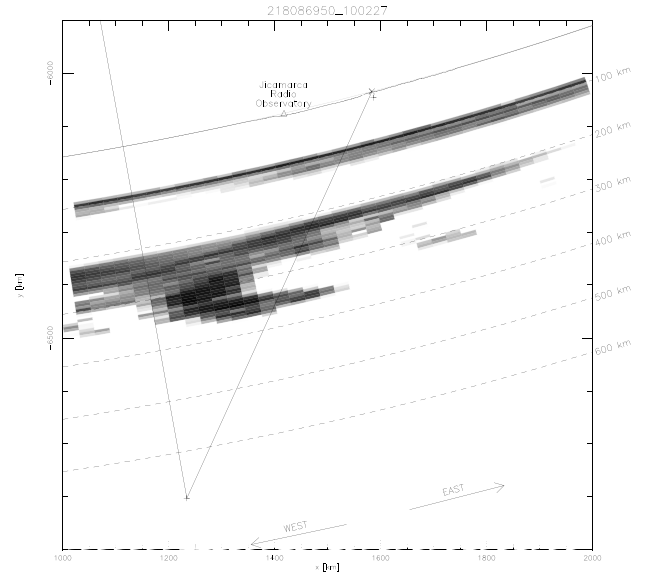


Fig. 18. RTI measurements by JULIA converted to the SAR acquisition geometry by means of (16) for ALPSRP218086950 data take.

estimate is similar to the full-band estimate (single-layer, $h_{\text{iono}} = 353$ km), but the velocity estimate is now more realistic (single-layer, $v_{\perp} = -99$ m/s). The inverted height and drift velocity from the red sector are $h_{\text{iono}} = 231$ km and $v_{\perp} = 246$ m/s. They are significantly different from the full-band estimates, and the velocity estimate appears to be strongly overestimated. However, the height estimates from the two sectors are within the range of heights provided by the ground measurements. As the yellow and orange solution bands are vertically oriented and quite parallel to each other, the velocity estimates (y -coordinate) become unstable, while the height estimates are relatively robust.

The equatorial spread F over the JRO is also monitored by measuring the Bragg-scattering from the irregular ionospheric structures at 50 MHz by the Jicamarca Unattended Long-term Investigations of the Ionosphere and Atmosphere (JULIA) instrument [2], [20]. JULIA records the range-time-intensity (RTI) measurements overnight [20]. For the validation of the SAR-derived ionospheric height estimates, JULIA’s RTI measurements are converted to spatial maps by converting time t to longitude λ

$$\lambda = (t - t_0)\omega + \lambda_0 \quad (16)$$

where λ_0 is the longitude of JRO, t_0 is the ALOS PALSAR acquisition time, and $\omega = 7.292 \times 10^{-5} \text{ s}^{-1}$ is the angular velocity of earth’s rotation. This conversion reconstructs the spatial distribution of the ionospheric irregularities at the ALOS scene acquisition time t_0 . It is exact at λ_0 ($=t_0$), and becomes more and more inaccurate with changing longitude as the measurements at an latitude λ do not longer correspond to the scene acquisition time t_0 , but to a previous (or later) $(\lambda - \lambda_0)/\omega$ [21].

Fig. 18 shows the ionospheric irregularities measured by JULIA during the ALOS PALSAR (ALPSRP218086950) acquisition time according to (16). It is a xy plane cross section in an earth-centered, earth-fixed (ECEF) coordinate

system where the z -coordinate corresponds to the latitude of the JRO. The arc on the top represents the cross section of the earth's surface, and the altitude contours are given by the dashed contours. As the plane is seen from north to south, the east direction is on the right and the west direction on left. The satellite location at the acquisition time and the scene center are not placed in the xy plane hosting JRO. The "+" indicate the projections of the satellite and the scene center on the xy plane, respectively, while the "x" indicates the projection of the scene center on the earth's surface on the xy plane. The JULIA measurements are performed along the normal direction at JRO, which also lies not on the xy plane. But as the ionospheric irregularities are aligned to the geomagnetic field which is almost perpendicular to xy plane at this latitude, the RTI map on xy plane has only small deviations. The longitude varies 10° in Fig. 18, corresponding to 40 min of earth's rotation.

In Fig. 18, the LOS of ALOS PALSAR intersects the ionospheric irregularities three times at 100, 220–270, and 350 km. The highest two layers are coinciding to the height estimates from the blue and red sectors, respectively. It is not clear why the thick and stronger middle layer (at 220–270 km) contributes with a weaker spectral power (see Fig. 16). The lowest irregularity layer appears consistently in most of the JULIA's measurements compared for this study and is not considered as a genuine disturbance source. At the same time, JULIA also measures the horizontal components of drift. However, because of its noisy behavior at this night, the velocity estimates are not compared.

V. CONCLUSION

A methodology to estimate the height of the "active" ionospheric layer and the drift velocity of the postsunset scintillations in the equatorial F region from the "stripe"-patterns induced in SAR images has been proposed and validated against reference measurements. First, the detection and "straightening" of the "stripe" patterns has been addressed. The detection of "stripe" patterns in many of the ALOS scenes investigated indicates that many more of the SAR images acquired in the equatorial postsunset sector are affected by scintillations than up to now assumed. In a second step, the orientation of the "stripe" pattern and its displacement across azimuth subband images has been interpreted by mapping the ionospheric irregularities and their drift into the SAR image geometry. Based on this the inversion equations for the height of the "active" ionospheric layer and the drift velocity of the scintillations have been established.

The obtained height estimates range between 100 and 350 km: 300 km (decreasing to 100 km at diminishing northern part) for the Amazon 2008 data set, 250–350 km for the Amazon 2009 data set, and 230–330 km for the Jicamarca data sets. The drift velocity estimates range between 100–200 m/s: 100–200 m/s for the Amazon data sets in 2008 and 2009, and 100 m/s for the Jicamarca 2008 data set and are in a good agreement with the estimates of previous studies (ca. 100 m/s around LT 22:30 [11] or up to 200 m/s measured in [4]). However, the Jicamarca 2010 data set shows a significant deviation: The single-layer (i.e., full-band)

estimation yields -100 m/s, while when assuming a two-layer ionosphere drifts of -50 and 250 m/s are obtained. The first one is too small and the second one is too large.

At the equator, for the right-looking ascending case the downward motion of the plasma irregularities compensates its eastward motion, while the upward motion exaggerates. Previous studies show that in the postsunset sector, the predominant vertical motion is downward (-20 to -30 m/s around 22:30 LT [11] and also in Table I). Therefore the range projected drift velocity is expected to be smaller than the eastward velocity of 100 to 200 m/s. The estimates obtained in this paper are in general, slightly larger than the ones reported in the literature. One possible explanation for this may be that the velocity measurement becomes instable when the geomagnetic field angle i becomes larger than ca. 10° and (11)–(14) becomes too similar. This may be the case for the Jicamarca 2010 data where the geomagnetic field angle $i = 12.2^\circ$ at 350 km. For the Amazon data set the geomagnetic field angle varies within $[-10^\circ, +10^\circ]$ (see Fig. 11) allowing the reliable velocity estimation.

A different possibility to interpret the obtained overestimates of the drift velocity is the decoupling of the ambient plasma and plasma irregularities. As the ambient ionosphere moves downward, the plasma irregularity ascends due to its lower density. Because the "stripe" patterns are associated with the low density plasma irregularities, the decoupled ascending irregularities might explain the overestimation of the drift velocity obtained.

The obtained results indicate the potential of space-borne SAR configurations toward the parametric monitoring of ionospheric structure and dynamics. However, due to their band-limited nature SAR configurations are sensitive only to a subset of the ionospheric structures. The diffraction pattern seen by a given SAR configuration is, at a certain range of altitudes, optimized to a given horizontal spectral component of the ionospheric irregularities. The understanding about which component of the ionosphere is responsible for which effect in the SAR image is not complete and remains to be established. For example, Carrano *et al.* [9] proposed, based on results of the spectral index analysis, a bottom side irregularity as the origin of the "stripe" pattern. However, the obtained height estimates of 300 km in our study indicate that the potential origin is higher than the bottom layer. Dedicated experiments combining SAR data acquisition with simultaneous ionospheric measurements are required to answer these questions.

ACKNOWLEDGMENT

The authors would like to thank B. W. Reinisch with the University of Massachusetts Lowell, Lowell, MA, USA, for making the ionogram data (<http://spase.info/VWO/NumericalData/GIRO/CHARS.PT15M>) and drift velocities measurements (<http://spase.info/VWO/DisplayData/GIRO/SKYMAP.PT15M>) available through Global Ionospheric Radio Observatory (<http://spase.info/SMWG/Observatory/GIRO>). The authors would like to thank JAXA, Tokyo, Japan, for providing the ALOS PALSAR and ALOS-2 data in the frame of the PI contracts 1478 and 3323. The JULIA radar measurements used in this study can be obtained

from the Madrigal database at <http://jro.igp.gob.pe>. The Jicamarca Radio Observatory is a facility of the Instituto Geofísico del Perú operated with support from the NSF AGS-1433968 through Cornell University, Ithaca, NY, USA.

REFERENCES

- [1] A. J. Scannapieco and S. L. Ossakow, "Nonlinear equatorial spread F," *Geophys. Res. Lett.*, vol. 3, no. 8, pp. 451–454, 1976, doi: 10.1029/GL003i008p00451.
- [2] M. C. Kelly, *The Earth's Ionosphere: Plasma Physics and Electrodynamics*, 2nd ed. San Diego, CA, USA: Academic, 2009.
- [3] B. G. Fejer, "Low latitude electrodynamic plasma drifts: A review," *J. Atmos. Terrestrial Phys.*, vol. 53, no. 8, pp. 677–693, Aug. 1991.
- [4] W. R. Coley and R. A. Heelis, "Low-latitude zonal and vertical ion drifts seen by DE 2," *J. Geophys. Res.*, vol. 94, no. A6, pp. 6751–6761, Jun. 1989.
- [5] B. G. Fejer, E. Kudeki, and D. T. Farley, "Equatorial F region zonal plasma drifts," *J. Geophys. Res.*, vol. 90, no. A12, pp. 12249–12255, Dec. 1985.
- [6] M. Shimada, Y. Muraki, and Y. Otsuka, "Discovery of anomalous stripes over the Amazon by the PALSAR onboard ALOS satellite," in *Proc. IGARSS*, Boston, MA, USA, Jul. 2008, pp. II-387–II-390.
- [7] F. J. Meyer, K. Chotoo, S. D. Chotoo, B. D. Huxtable, and C. S. Carrano, "The influence of equatorial scintillation on L-band SAR image quality and phase," *IEEE Trans. Geosci. Remote Sens.*, vol. 54, no. 2, pp. 869–880, Feb. 2015, doi: 10.1109/TGRS.2015.2468573.
- [8] J. Aarons, "Global morphology of ionospheric scintillations," *Proc. IEEE*, vol. 70, no. 4, pp. 360–378, Apr. 1982.
- [9] C. S. Carrano and K. M. Groves, R. G. Craton, "Simulating the impacts of ionospheric scintillation on L band SAR image formation," *Radio Sci.*, vol. 47, no. 4, p. RS0L20, Aug. 2013, doi: 10.1029/2011RS004956.
- [10] J. S. Kim, K. P. Papathanassiou, R. Scheiber, and S. Quegan, "Correcting distortion of polarimetric SAR data induced by ionospheric scintillation," *IEEE Trans. Geosci. Remote Sens.*, vol. 53, no. 12, pp. 6319–6335, Dec. 2015, doi: 10.1109/TGRS.2015.2431856.
- [11] B. G. Fejer, E. R. de Paula, S. A. González, and R. F. Woodman, "Average vertical and zonal F region plasma drifts over Jicamarca," *J. Geophys. Res., Space Phys.*, vol. 96, no. A8, pp. 13901–13906, Aug. 1991.
- [12] B. G. Fejer, B. D. Tracy, and R. F. Pfaff, "Equatorial zonal plasma drifts measured by the C/NOFS satellite during the 2008–2011 solar minimum," *J. Geophys. Res., Space Phys.*, vol. 118, no. 6, pp. 3891–3897, Jun. 2013.
- [13] A. Bhattacharyya, S. Basu, K. M. Groves, C. E. Valladares, and R. Sheehan, "Dynamics of equatorial F region irregularities from spaced receiver scintillation observations," *Geophys. Res. Lett.*, vol. 28, no. 1, pp. 119–122, Jan. 2001.
- [14] H. Kil, P. M. Kintner, E. R. de Paula, and I. J. Kantor, "Global positioning system measurements of the ionospheric zonal apparent velocity at Cachoeira Paulista in Brazil," *J. Geophys. Res., Space Phys.*, vol. 105, no. A3, pp. 5317–5327, Mar. 2000.
- [15] E. Thébaud *et al.*, "International geomagnetic reference field: The 12th generation," *Earth, Planets Space*, vol. 67, no. 1, p. 79, May 2015.
- [16] T. G. Farr *et al.*, "The shuttle radar topography mission," *Rev. Geophys.*, vol. 45, no. 2, p. RG2004, 2007, doi: 10.1029/2005RG000183.
- [17] J. S. Kim and K. P. Papathanassiou, "On the separation of dynamic scattering and ionospheric effects in SAR data," in *Proc. POLinSAR*, Frascati, Italy, 2015, pp. 1–8.
- [18] P. Wessel and W. H. F. Smith, "A global, self-consistent, hierarchical, high-resolution shoreline database," *J. Geophys. Res., Solid Earth*, vol. 101, no. B4, pp. 8741–8743, Apr. 1996.
- [19] B. W. Reinisch and I. A. Galkin, "Global ionospheric radio observatory (GIRO)," *Earth, Planets, Space*, vol. 63, no. 4, pp. 377–381, 2011, doi: 10.5047/eps.2011.03.011.
- [20] D. L. Hysell and J. D. Burcham, "Long term studies of equatorial spread F using the JULIA radar at Jicamarca," *J. Atmos. Solar-Terrestrial Phys.*, vol. 64, nos. 12–14, pp. 1531–1543, 2002.
- [21] J. S. Kim, H. Sato, and K. Papathanassiou, "Validation of ionospheric mapping by means of SAR through ground based radar measurements," in *Proc. EUSAR*, Hamburg, Germany, Jun. 2016, pp. 1–6.



Jun Su Kim was born in Busan, South Korea, in 1982. He received the bachelor's and master's degrees in earth environmental sciences from Seoul National University, Seoul, South Korea, in 2004 and 2007, respectively, and the Ph.D. degree from the Department of Civil, Environmental, and Geomatic Engineering, Swiss Federal Institute of Technology in Zurich, Zurich, Switzerland, in 2014.

Since 2008, he has been with the German Aerospace Center (DLR-HR), Microwaves and Radar Institute, Wessling, Germany. His research interest includes the development of parametric monitoring method of the ionosphere using synthetic aperture radar (SAR) and SAR polarimetry.



Konstantinos P. Papathanassiou (A'01–M'06–SM'09–F'13) received the Dipl.Ing. (Hons.) and Dr. (Hons.) degrees from the Department of Physics, Graz University of Technology, Graz, Austria, in 1994 and 1999, respectively.

From 1992 to 1994, he was with the Institute for Digital Image Processing (DIBAG), Joanneum Research, Graz. From 1995 to 1999, he was with the German Aerospace Center (DLR-HR), Microwaves and Radar Institute, Wessling, Germany. From 1999 to 2000, he was a European Union Post-Doctoral Fellow with Applied Electromagnetics, St. Andrews, U.K. Since 2000, he has been a Senior Scientist with DLR-HR, leading the Information Retrieval Research Group. He has authored or co-authored more than 100 publications in international journals, conferences, and workshops. His research interests include polarimetric and interferometric processing and calibration techniques, polarimetric synthetic aperture radar (SAR) interferometry, and the quantitative parameter estimation from SAR data, as well as in SAR mission design and SAR mission performance analysis.

Dr. Papathanassiou was a recipient of the IEEE GRSS IGARSS Symposium Prize Paper Award in 1998, the Best Paper Award of the European SAR Conference in 2002, the DLR Science Award in 2002, and the DLR Senior Scientist Award in 2011.



Hiroatsu Sato received the bachelor's and master's degrees in physics from Kyoto University, Kyoto, Japan, in 2003 and 2006, respectively, and the Ph.D. degree from the Department of Physics, University of Oslo, Oslo, Norway, in 2011, with a thesis on space plasma physics.

Since 2013, he has been with the German Aerospace Center (DLR), Institute of Communications and Navigation, Neustrelitz, Germany. His research interests include ionospheric effects on satellite signals, ionospheric disturbances, and space weather.



Shaun Quegan (M'90) received the B.A. and M.Sc. degrees in mathematics from the University of Warwick, Coventry, U.K., in 1970 and 1972, respectively, and the Ph.D. degree from The University of Sheffield, Sheffield, U.K., in 1982.

From 1982 to 1986, he was a Research Scientist with the Marconi Research Centre, Great Baddow, U.K., and led the Remote Sensing Applications Group from 1984 to 1986. He established the SAR Research Group at The University of Sheffield in 1986, whose success led to his professorship awarded in 1993. In the same year, he helped inaugurate the Sheffield Centre for Earth Observation Science, of which he remains the Director. In 2001, he became the Director of the Centre for Terrestrial Carbon Dynamics, U.K. National Environmental Research Council. This multi-institutional center is concerned with assimilating earth observation and other data into process models of the land component of the carbon cycle and now forms part of the U.K. National Centre for Earth Observation. His research interests include physics, systems, and data analysis aspects of radar remote sensing are now subsumed in the more general aim of exploiting many sorts of electro-optic technology to give greater quantitative understanding of the carbon cycle.